ARTICLE OPEN

Check for updates

Anisotropic positive linear and sub-linear magnetoresistivity in the cubic type-II Dirac metal Pd_3In_7

Aikaterini Flessa Savvidou[1,2], Andrzej Ptok [3], G. Sharma[4], Brian Casas[1], Judith K. Clark[5], Victoria M. Li[5], Michael Shatruk[5], Sumanta Tewari [6] and Luis Balicas [1,2✉]

We report a transport study on Pd_3In_7 which displays multiple Dirac type-II nodes in its electronic dispersion. Pd_3In_7 is characterized by low residual resistivities and high mobilities, which are consistent with Dirac-like quasiparticles. For an applied magnetic field (μ_0H) having a non-zero component along the electrical current, we find a large, positive, and linear in μ_0H longitudinal magnetoresistivity (LMR). The sign of the LMR and its linear dependence deviate from the behavior reported for the chiral-anomaly-driven LMR in Weyl semimetals. Interestingly, such anomalous LMR is consistent with predictions for the role of the anomaly in type-II Weyl semimetals. In contrast, the transverse or conventional magnetoresistivity (CMR for electric fields $\mathbf{E} \perp \mu_0H$) is large and positive, increasing by $10^3 - 10^4$ % as a function of μ_0H while following an anomalous, angle-dependent power law $\rho_{xx} \propto (\mu_0H)^n$ with $n(\theta) \leq 1$. The order of magnitude of the CMR, and its anomalous power-law, is explained in terms of uncompensated electron and hole-like Fermi surfaces characterized by anisotropic carrier scattering likely due to the lack of Lorentz invariance.

INTRODUCTION

Triggered by the discovery of topological insulators[1], the condensed matter community has, in recent years, focused intensively on the topological nature of the electronic band structure of materials. The subsequent discovery of Dirac[2,3] and Weyl semimetals[4,5] as well as higher order topological systems[6] continues to strengthen this interest. In particular, the study of Dirac materials is at the forefront of research, ranging from *d*-wave superconductors[7], graphene[8], bulk semi-metallic systems such as Cd_3As_2[9], to Lorentz invariance violating systems that are characterized by tilted Dirac/Weyl cones, or the so-called type-II Dirac/Weyl compounds[10–12].

This intense interest in topological compounds relies on the prediction and observation of unreported phenomena such as a fermion chirality-dependent circular galvanometric effect[13–15], a Hall-effect in the absence of time-reversal symmetry[16,17], or the prediction for an anomalous magnetoresistivity resulting from the chiral anomaly among Weyl nodes[18–24]. In conventional or three-dimensional type-I Dirac/Weyl systems, the chiral or axial anomaly is predicted[18–24] to provide an additional positive contribution to the longitudinal magneto-conductivity (LMC) of semimetallic systems when a component of the external magnetic field μ_0H is aligned along the electric field $\mathbf{E}$ driving the current density $\mathbf{j}$. Essentially, μ_0H favors one fermion chirality to the detriment of the other inducing a net charge transfer, or an axial current between nodes.

In type-II Dirac/Weyl systems, the existence of tilted Dirac/Weyl cones also leads to an anomalous contribution to the LMC[25]. It was originally predicted[25] to occur when μ_0H is oriented within a cone in $k-$space satisfying the condition $|T(\mathbf{k})| > |U(\mathbf{k})|$, where $|T(\mathbf{k})|$ and $|U(\mathbf{k})|$ represent the kinetic and potential energy components of the linear energy dispersion. Subsequent work found that this anomaly introduces a linear in field contribution to

the LMC for fields applied along the tilt direction, but a quadratic one under perpendicularly applied fields[26,27]. Recent studies paint a more nuanced and complex scenario, with the anomaly leading even to a positive contribution to the LMR, in contrast to the proposed positive contributions to the LMC[28–30]. Furthermore, according to refs. [28–30] the observation of positive versus negative LMR would depend on the tilt direction of the Dirac/Weyl cones, the level of tilting, their relative inclination, relative separation, the orientation of μ_0H relative to the vector connecting them, and the strength of intervalley scattering. Throughout this text, conventional magnetoresistivity (CMR) refers to a configuration where $\mathbf{j} \perp \mu_0H$

Type-II Weyl semimetals provide another interesting scenario due to the presence of both electron and hole pockets coexisting with the Weyl points on the Fermi surface. As observed in the type-II Weyl semimetal WTe_2[31], a near exact compensation of electron and hole pockets may result in a very large and non-saturating magnetoresistivity that varies quadratically with the applied field. Here, we shall show that even uncompensated electron and hole pockets can yield significant CMR and exhibit an anomalous power law dependence on the magnetic field: $\rho_{xx} \propto (\mu_0H)^n$, with $n \leq 1$. We thereby investigate both the unconventional LMR and the anomalous CMR that results from the axial anomaly acting on a type-II Dirac/Weyl system that lacks carrier compensation and is characterized by anisotropic carrier scattering on its Fermi surfaces.

To understand the influence of electronic topology on the magnetoresistivity, a number of Dirac/Weyl systems have been recently studied, including proposed type-II Weyl semimetals such as WTe_2[31] or NbP[32], three-dimensional type-I Dirac semimetals such as Cd_3As_2[9] or Na_3Bi[3], type-I Weyl semimetallic systems such as $TaAs$[4,5] and many others. These materials exhibit high carrier mobilities[9], in some cases very large, and linear CMR[9,31,33], and

[1]National High Magnetic Field Laboratory, Florida State University, Tallahassee 32310 FL, USA. [2]Department of Physics, Florida State University, Tallahassee 32306 FL, USA. [3]Institute of Nuclear Physics, Polish Academy of Sciences, W. E. Radzikowskiego 152, Kraków PL-31342, Poland. [4]School of Physical Sciences, Indian Institute of Technology Mandi, Mandi 175005 H.P., India. [5]Department of Chemistry and Biochemistry, Florida State University, Tallahassee 32306 FL, USA. [6]Department of Physics and Astronomy, Clemson University, Clemson 29634 SC, USA. ✉email: balicas@magnet.fsu.edu
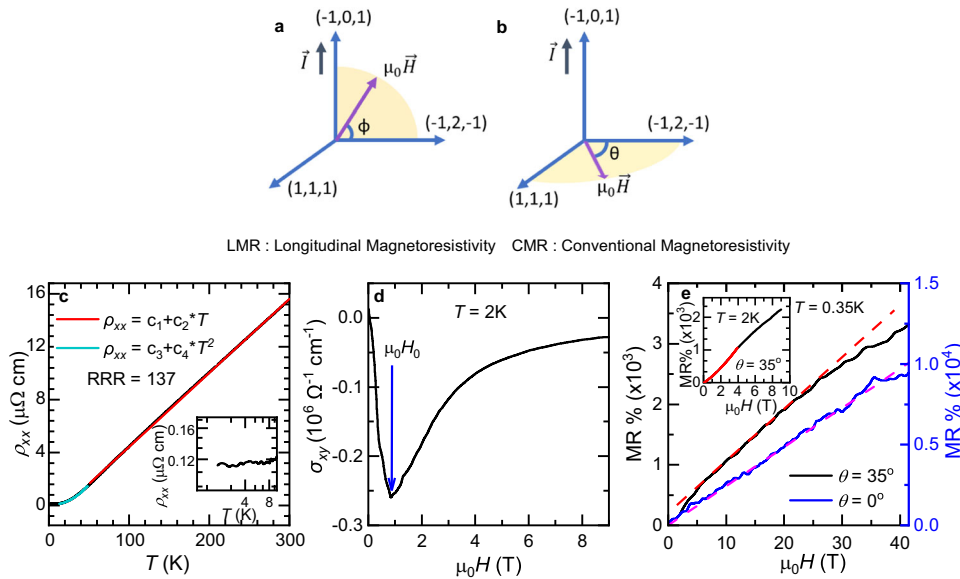
Fig. 1 Linear and sub-linear magnetoresistivity in Pd₃In₇. **a** Sketch depicting the planes of rotation of the magnetic field μ_0H, from $I \perp \mu_0H$ to $I \| \mu_0H$ (longitudinal magnetoresistivity configuration or LMR), as a function of the angle ϕ. I is the electrical current. **b** Sketch illustrating sample rotation under μ_0H, where I is kept $\perp \mu_0H$ and the angle θ is varied (conventional magnetoresistivity configuration or CMR) **c** Electrical resistivity ρ_{xx} of Pd₃In₇ as a function of the temperature T. For $T > 50$ K, ρ_{xx} displays a linear dependence on T (red line is a linear fit), while ρ_{xx} exhibits a quadratic behavior (cyan line is a fit) for $T \leq 50$ K. Inset: ρ_{xx} in a magnified scale illustrating the residual resistivity $\rho_0 \simeq 110$ nΩ cm. **d** Hall conductivity σ_{xy} as a function of μ_0H, displaying a minimum at $\mu_0H_0 = 0.84$ T. **e** Magnetoresistivity MR as a function of μ_0H for 3 T $\leqq \mu_0H \leqq 41.5$ T. Blue and black lines correspond to the experimental data for $\theta = 0°$ and $\theta = 35°$, respectively. Dashed magenta line corresponds to a linear fit of the $\theta = 0°$ data for the entire field range, while red dashed line indicates the deviation of the black line with respect to linear behavior. Inset: MR as a function of μ_0H, for fields up to $\mu_0H = 9$ T. Red line is a fit of the data for $\mu_0H < 4$ T to MR $= d_1 + d_2(\mu_0H) + d_3(\mu_0H)^2$, where d_2 and d_3 are coefficients of the linear and quadratic terms, respectively.

evidence for the chiral anomaly (negative LMR)[3–5]. Experimentally, there have been few reports on the transport properties of pure type-II Dirac systems, with the CMR of systems like NiTe₂ or SrAgB displaying linear[34,35], and in occasions a sublinear[36] dependence on field. And systems displaying substantial residual resistivities, i.e., tens of μΩ cm like Ir₂In₈S, claimed to display power laws in field with exponents ranging between 1 and 2[37]. It is therefore important to expose the transport properties of very clean and isotropic type-II Dirac systems that do not display any type of ordering.

Here, we focus on compounds belonging to the Ir₃Ge₇ family of cubic structures that are known to display a remarkable compositional variability. Chemical substitutions can vary the electron count widely leading to semiconductors like Mo₃Sb₅Te₂[38], metals like Pd₃In₇, and even superconductors such as Mo₃Sb₇[39]. Metallic compounds like Pd₃In₇ or Pt₃In₇ have already been previously predicted to be topologically non-trivial[40]. Furthermore, the electronic band structure of the newly discovered Rh₃In₃.₄Ge₃.₆ compound, which belongs to the same structural family, displays multiple band crossings close to the Fermi energy ε_F, leading to type-I, type-II, and even type-III Dirac nodes[41]. Our calculations reveal the existence of multiple type-II Dirac nodes near the Fermi level of Pd₃In₇. In this study, we find Pd₃In₇ to display a very low residual resistivity, high carrier mobilities due to low carrier effective masses, and pronounced CMR, which are the transport hallmarks of Dirac-like quasiparticles. Remarkably, this compound tends to display linear CMR but with a superimposed conventional quadratic in-field term[42] at rather low fields. This dependence crosses over to an angle-dependent power law $\rho_{xx} \propto (\mu_0H)^n$ at higher fields, with $n < 1$, except for a very specific magnetic field orientation where $n = 1$ over the entire field range. In a LMR configuration, that is for **j**$\|\mu_0$**H**, we do not observe the conventional saturating magnetoresistance[43]. Instead, a positive LMR is observed under fields as high as $\mu_0H = 35$ T.

Given that Pd₃In₇ is a clean system that remains well below the quantum limit under available magnetic fields, and displays no magnetic or electronic order, we conclude that its anomalous LMR results from the axial anomaly among type-II Dirac/Weyl nodes. In contrast, the sublinear dependence of the CMR on the magnetic field is explained as a multi-band effect due to the presence of uncompensated electron and hole pockets of distinct carrier mobilities. The angular dependence of the power-law exponent as the field is rotated is attributed to a pronounced angle-dependent Zeeman effect resulting from the large and anisotropic value of the Landé g-factor in Pd₃In₇. This is likely to lead to an anisotropic modification of the geometry of the Fermi surface(s) changing the scattering rates or mobilities of electrons and holes on them, as the field is rotated relative to the crystallographic axes. This effect might be pronounced on the smallest Fermi surfaces. We argue that this might explain the experimentally observed angular dependence of the exponent $n(\theta)$ in an uncompensated metal like Pd₃In₇.

RESULTS

Anomalous magnetoresistivity in Pd₃In₇

Figure 1a, b provide a schematic depicting the planes of rotation of the magnetic field relative to the crystallographic axes, as well as the definition of the angles ϕ and θ, used for measuring the longitudinal and conventional magnetoresistivities, respectively. The planes of rotation were defined by the natural morphology of the measured single crystals. The resistivity ρ_{xx} as a function of the temperature T for a Pd₃In₇ single crystal is displayed in Fig. 1c, revealing metallic behavior with a linear dependence on T (red line is a linear fit) for $T > 50$ K. For $T \leqq 50$ K, it follows a quadratic dependence on T (cyan line is a fit to a T^2 term), indicating Fermi-liquid behavior. The high value of the residual resistivity ratio, $RRR = (\rho_{xx}(300K) - \rho_{xx}(2K))/\rho_{xx}(2K) \simeq 137$, as well as the low residual resistivity $\rho_0 \simeq 110$ nΩ cm (inset in Fig. 1c), point to the

very high crystalline quality of the sample, or its low level of disorder. To evaluate the mean transport mobility μ_{tr} of our crystals, we calculated the Hall conductivity σ_{xy} based on the magnetoresistivity ρ_{xx} and the Hall resistivity ρ_{xy}:

$$\sigma_{xy} = -\frac{\rho_{xy}}{\rho_{xx}^2 + \rho_{xy}^2} \qquad (1)$$

σ_{xy} as a function of $\mu_0 H$ is plotted in Fig. 1d. From σ_{xy}, we can extract the mean transport mobility of the charge carriers: $\mu_{tr} = (\mu_0 H_0)^{-1} = 1.2 \times 10^4$ cm^{2}V^{-1}s^{-1}. This value is comparable to those extracted from type-II Dirac semimetallic systems like MoTe$_2$[44] or WP$_2$[45], which are characterized by extremely high magnetoresistivities, but considerably smaller than those values reported for Dirac nodal line systems like ZrSiSe[46], and over two orders of magnitude smaller than the mobilities reported for the Dirac semimetal Cd$_3$As$_2$[9]. In contrast, Pd$_3$In$_7$ is a metal characterized by large Fermi surfaces (or large carrier densities) as discussed below, or is not a nearly compensated semimetal as is the case for those systems. The mean free path $l_0 = v_F \mu_{tr} m^\star / e$ (v_F is the Fermi velocity and e the electron charge) can be estimated from the effective mass $m^\star$ extracted from the de Haas-van-Alphen (dHvA) oscillations (discussed below) and the average transport mobility μ_{tr}, yielding Fermi surface cross-sectional area dependent values $l_0 \approx 0.88 - 4.75 \, \mu$m at $T = 0.35$ K. The low value of the residual resistivity ρ_0 and the large values of l_0 clearly indicate that impurities have a negligible role on the transport properties of Pd$_3$In$_7$. This is an important point for the subsequent discussions.

The magnetic field dependence of the magnetoresistivity MR depends on the angle of rotation relative to the main crystallographic axes. The MR, in %, is defined as:

$$MR = \frac{\rho_{xx}(\mu_0 H) - \rho_{xx}(0)}{\rho_{xx}(0)} \cdot 100 \qquad (2)$$

As depicted in Fig. 1a to measure LMR, the magnetic field $\mu_0 H$ was rotated from an initial position perpendicular to the current I or $\phi = 0°$, with $\mu_0 \mathbf{H} \| (-1, 2, -1)$, and towards $\mu_0 \mathbf{H} \| \mathbf{I} \| (-1, 0, 1)$ or $\phi = 90°$. For the conventional magnetoresistivity or CMR, $\mu_0 H$ remains perpendicular to the current I over the entire angular range, with $\theta = 0°$ corresponding to $\mu_0 \mathbf{H} \| (-1, 2, -1)$ and $\theta = 90°$ to $\mu_0 \mathbf{H} \| (1, 1, 1)$ (Fig. 1b). The magnetic field was rotated within these specific crystallographic planes due to the morphology of the as-grown crystals. Electrical contacts were placed on the largest as-grown crystalline surface. Previously, the crystal was polished on the opposite surface to decrease its thickness. In Pd$_3$In$_7$ crystals, planes perpendicular to the main crystallographic axes, i.e., (1,0,0), (0,1,0) or (0,0,1), yield rather small surfaces which precluded transport measurements with magnetic fields applied along them. The lowest temperatures were chosen to minimize the role of phonons.

As seen in the inset of Fig. 1e, most field orientations lead to a similar MR behavior, quadratic in field dependence at low fields and sublinear at higher fields (Fig. 1e, black trace). A sublinear MR in a very clean system, that displays several Dirac crossings in its band structure (as we show below), has not been thoroughly exposed and characterized. In the inset of Fig. 1e, or for $\theta = 35°$, the quadratic in field response is observed for $\mu_0 H < 4$ T where the MR is fitted (red line) to a combination of linear and quadratic components: MR $= d_1 + d_2(\mu_0 H) + d_3(\mu_0 H)^2$. At the same angle and for $\mu_0 H > 4$ T, the MR becomes sub-linear in $\mu_0 H$, but as seen in Fig. 1e for the black trace, it does not saturate even under fields as large as $\mu_0 H = 41.5$ T. The red dashed line is a guide to eye indicating the deviation of the raw data with respect to linear behavior.

Over a broad range of fields the MR can be fitted to a power law (red line in Supplementary Fig. 4), i.e., MR $= a(\mu_0 H)^n$ with $n < 1$. Remarkably, and as seen in Fig. 1e, blue line, when the angle of rotation is $\theta = 0°$ the MR displays a linear dependence on $\mu_0 H$ from $\mu_0 H = 0$ T all the way up to $\mu_0 H = 41.5$ T. The magenta dashed line

is a linear fit illustrating this point. At the highest fields, the observed deviations with respect to linearity are attributable to the Shubnikov-de Haas oscillations. This linear dependence is observed only at this precise orientation, whereas for all other angles the MR displays a combination of linear and quadratic terms for $\mu_0 H < 4$ T, followed by sublinear dependence at higher fields. Notice that the linear MR of Pd$_3$In$_7$ is far more pronounced than that of Ag$_{2+\delta}$Se, a compound previously proposed as a possible megaGauss sensor[47], and extends to higher fields. This linearity extends to higher temperatures and follows Kohler's scaling[48], as seen in Supplementary Fig. 5. The LMR displays a positive, and nearly linear in field behavior over the entire ϕ range. In Supplementary Fig. 6, the LMR is displayed for $\mu_0 \mathbf{H} \| \mathbf{I}$, or $\phi = 90°$.

This linear (and sublinear) in magnetic field dependence for the CMR contrasts markedly with previous reports for type-I Weyl semimetals, i.e., a $(\mu_0 H)^2$ dependence followed by a linear one at high fields[49]. For compensated semimetals, the dependence on the magnetic field is quadratic over the entire field range[31,49]. As we discuss below, the linear as well as sublinear dependence on the magnetic field is explained as a multi-band effect due to the presence of uncompensated electron and hole pockets in the Type-II Dirac metal Pd$_3$In$_7$.

For an axis of rotation that maintains the magnetic field perpendicular to the electrical current, i.e., for a configuration that maintains the Lorentz force at its maximum value throughout the entire angular range, we observe an anisotropic fourfold, butterfly-like, angular MR (Fig. 2a, b). Figure 2b shows the CMR for various magnetic fields, showing an increase of ~1000% under $\mu_0 H = 9$ T. Figure 2a corresponds to a polar plot of the CMR in units of %. From the polar plot one observes two- and fourfold symmetries, as well as dips in the CMR at $\theta = 0°$, 30° and 90°. It is important to emphasize that this angular structure cannot be attributed to the superimposed Shubnikov-de Haas oscillations. Supplementary Fig. 1 displays the CMR as a function of $\mu_0 H$ for several values of θ. At the highest fields, its background, upon which the oscillations are superimposed, displays two clear minima at $\theta \sim 30°$ and $\theta \sim 55°$. This confirms the intrinsic origin of the angular structure in the CMR that originates the butterfly like magnetoresistivity seen at lower fields, albeit over the entire angular range the current is always maintained perpendicular to the field.

For a rotation starting from $\mathbf{I} \perp \mu_0 \mathbf{H}$ or $\phi = 0°$ tilting towards $\phi = 90°$ or $\mathbf{I} \| \mu_0 \mathbf{H}$, thus modulating the strength of the Lorentz force, the MR is shown in Fig. 2c. As expected, for $\phi = 0°$ the MR reaches its maximum value of 7500% under $\mu_0 H = 35$ T, decreasing as the angle increases or as the Lorentz force decreases. Nevertheless, in the region between $\phi = 30°$ and $\phi = 55°$, the MR displays a second maximum whose origin remains to be understood. This so-called butterfly magnetoresistivity, was previously reported for the ZrSiS family of compounds and attributed to charge carriers initially exploring topologically trivial orbits on the Fermi surface that become non-trivial as the magnetic field rotates with respect to the main crystallographic axes[50]. Subsequent work concluded the existence of an anisotropic scattering rate on its Fermi surface that is probed by the electronic orbits upon rotation of the magnetic field[46].

To further expose the sublinear magnetoresistivity in Pd$_3$In$_7$, we plot in Fig. 3a and b the power exponent n as well as the coefficient a respectively, extracted by fitting the raw MR as a function of $\mu_0 H$ (Fig. 1e), measured at several angles, to the function MR $= a(\mu_0 H)^n$. For $\theta = 0°$, we obtain $n = 1$ but it progressively decreases as the θ increases, displaying a minimum $n \simeq 0.7$ around $\theta = 55°$–60°. In contrast, the coefficient a displays a maximum around this angular range, increasing by nearly 250% relative to its value at 0°. The power law exponent was also calculated through the derivative of $\rho_{xx} = \rho_0 + a(\mu_0 H)^n$, i.e., $n = \partial \ln(\rho_{xx} - \rho_0)/\partial \ln(\mu_0 H)$, in order to expose its field and angular dependence. In Fig. 3c and d, we plot n for two distinct crystallographic planes of rotation of $\mu_0 H$ relative to I. In Fig. 3c, $\mathbf{I}$ is
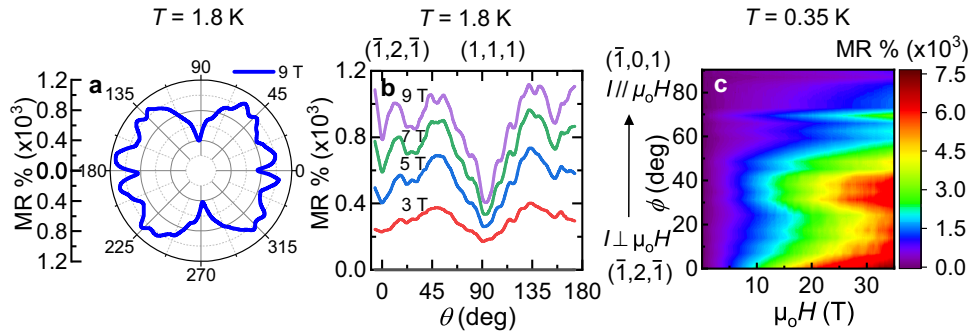
Fig. 2 Butterfly magnetoresistivity in cubic Pd₃In₇. a Polar plot of the magnetoresistivity MR at $T = 1.8$ K as a function of θ yielding an anisotropic butterfly-like angular dependence under a magnetic field $\mu_0 H = 9$ T. I is maintained $\perp$ to $\mu_0 H$ throughout the entire angular range. **b** Magnetoresistivity (MR) as a function of θ from 0°, or $\mu_0 H \| (-1, 2, -1)$ direction, to $\theta = 90°$ which corresponds to the $\mu_0 H \| (1, 1, 1)$ orientation, for different values of $\mu_0 H$. Throughout the whole rotation at a temperature $T = 1.8$ K, I is kept $\perp \mu_0 H$. A $\Delta\theta = 90°$ periodicity is observed at low fields, i.e., under $\mu_0 H = 3$ T, when the amplitude of the Shubnikov de Haas oscillations is quite small, implying that they are not responsible for it. **c** Color plot revealing the anisotropy of the MR at $T = 0.35$ K as a function of both angle and field, from $\theta = 0°$ or $I \perp \mu_0 H$, to 90° corresponding to $I \| \mu_0 H$.
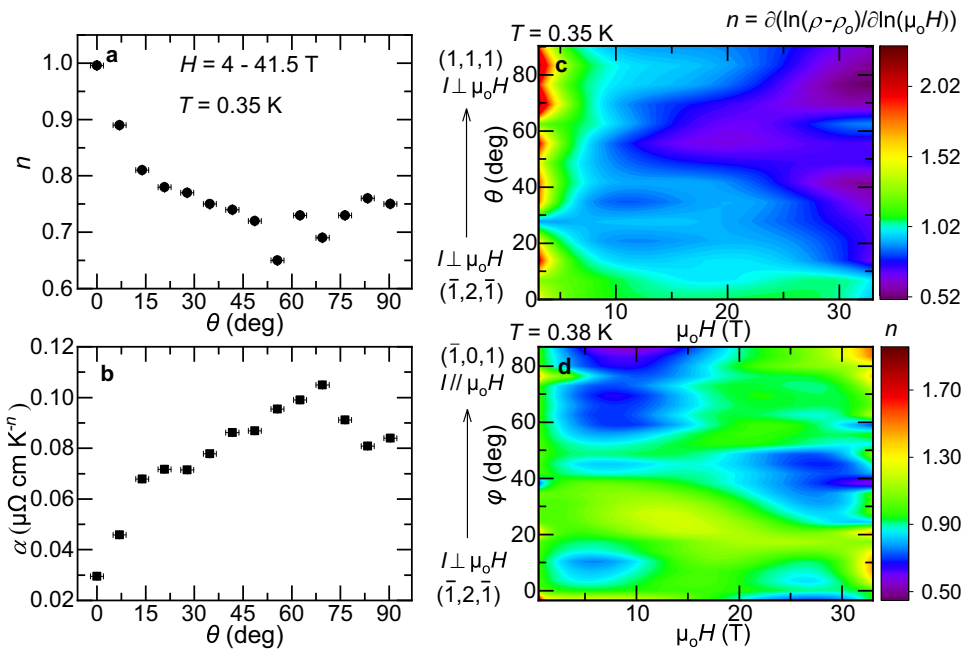

Fig. 3 Power law behavior of the magnetoresistivity of Pd₃In₇. a Power law coefficient n, in MR $\propto \alpha(\mu_0 H)^n$, as a function of the angle θ. Intriguingly, n reveals a minimum around $\theta = 60°$. **b** Coefficient α as a function of θ. Notice how α increases by a factor ~3 as θ exceeds 60°. **c** Color plot of the power coefficient n at $T = 0.35$ K, extracted from the relation $n = \partial \ln(\rho_{xx} - \rho_0) / \partial \ln(\mu_0 H)$, as a function of θ and $\mu_0 H$, for $I \perp \mu_0 H$ throughout the whole angular range. **d** Color plot of the power law coefficient n at $T = 0.38$ K, as a function of ϕ and $\mu_0 H$, from $\phi = 0°$, or $I \perp \mu_0 H$, to $\phi = 90°$, or $I \| \mu_0 H$.

kept $\perp \mu_0 H$ while $\mu_0 H$ rotates, or the angle θ is varied, as seen in Fig. 1b. The plot reveals $n = 2$ for $\mu_0 H < 4$ T, which becomes $n \sim 1$ for $4 \leq \mu_0 H \leq 10$ T. Above 10 T, n takes values $0.5 \leq n \leq 0.9$, for all angles excluding $\theta = 0°$. In contrast, when the current is rotated from $I \perp \mu_0 H$ to $I \| \mu_0 H$, $n \approx 1$ is extracted for the entire angular range, see Fig. 3d. In this panel, deviations with respect to $n = 1$ result from noise in the derivative due, for example, to the superimposed Shubnikov-de Haas oscillations. Both sets of measurements were performed on the same crystal, with the electrical contacts attached to the same crystallographic plane. The raw magnetoresistivity data $\rho_{xx}(\mu_0 H)$ for multiple values of both angles ϕ and θ, are presented in Supplementary Figs. 1 and 2 in the SI file. Small differences between distinct $\theta = 0°$ and $\phi = 0°$ traces shown in the main text and in the SI file, are attributable to the backlash of the mechanical rotator used for the experiments, i.e., $\Delta\theta \approx 1°$ and $\Delta\phi \approx 1°$. The important point is that the power law exponent of the magnetoresistivity remains at a value $n = 1$, or

well below it, as the field perpendicular to the current increases, displaying a quadratic term only at the lowest fields. Below, we argue that sublinear behavior is expected for a non carrier compensated system with both types of carriers having distinct mobilities. In contrast, the linear behavior for the LMR can result from the chiral anomaly among type-II Dirac nodes. Notice, that this unconventional magnetotransport behavior, precludes a reliable extraction of carrier densities and mobilities. This would require a simultaneous fitting of both the Hall-effect and the MR to semiclassical equations, which cannot describe the linear magnetoresistivity over the entire field range.

Band structure calculations and Fermi surface through the de Haas-van Alphen effect

We proceed to evaluate the geometry of the Fermi surface (FS) of Pd₃In₇ through the de Haas-van Alphen (dHvA) effect, in an
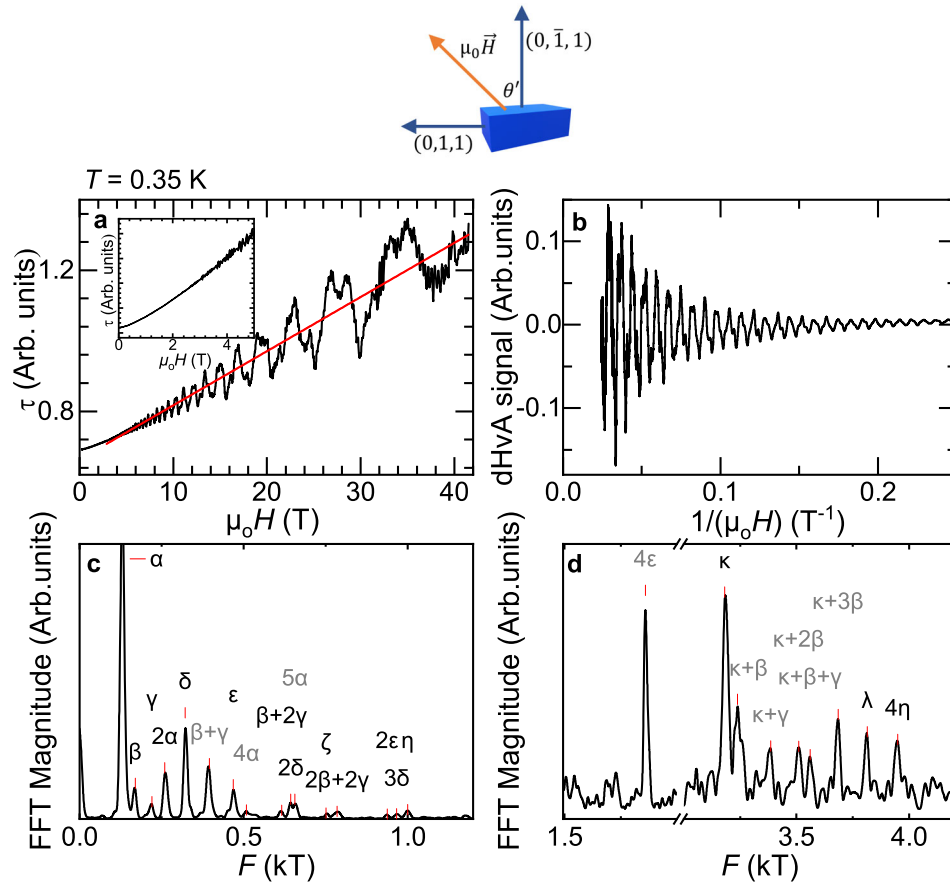
Fig. 4 De Haas-van Alphen effect in Pd$_3$In$_7$. a Magnetic torque τ at $T = 0.35$ K and as a function of $\mu_0 H$ for the angle $\theta' = 0°$, where θ' is the angle between $\mu_0 H$ and the $(0, -1, 1)$ direction. Red line is a polynomial fit to the background. **b** Superimposed de Haas van Alphen (dHvA) signal, as extracted from the magnetic torque in panel a as a function of inverse magnetic field $(\mu_0 H)^{-1}$. **c, d** Fast Fourier Transform (FFT) of the dHvA signal in (**b**), showing peaks at low and high frequencies that correspond to different extremal cross-sectional areas of the Fermi surface labeled with Greek letters. Peaks labeled by gray colored letters are likely harmonics of the fundamental frequencies, or their combination.

attempt to correlate its geometry with the one predicted by band structure calculations. The magnetic torque, $\tau = V\mathbf{M} \times (\mu_0 \mathbf{H})$, where V is the volume of the sample and M its magnetization, is shown in Fig. 4a as a function of the magnetic field. The sample was rotated according to the sketch in Fig. 4 starting with $\mu_0\mathbf{H}\|(0, -1, 1)$ corresponding to $\theta' = 0°$ and ending with $\mu_0\mathbf{H}\|(0, 1, 1)$ or $\theta' = 90°$. This particular plane of rotation was defined by the geometry of the sample given that its $(0, -1, 1)$ plane was the largest. The crystal was first characterized via a 4-probe resistivity measurement, before it was cut for the magnetic torque magnetometry. As seen in Fig. 4a, one observes oscillations in τ at $T = 0.35$ K due to the dHvA effect, starting at ~2–3 T, which implies carrier mobilities exceeding 3000 cm^2 V^{-1}s^{-1}. It turns out that this value is smaller than μ_{tr}, but it could result from the inherent lack of sensitivity of the torque technique at the lowest fields. The oscillatory component, or the dHvA signal, which is obtained after subtracting the background through a polynomial fit, is plotted as a function of inverse magnetic field $(\mu_0 H)^{-1}$ in Fig. 4b. Figure 4c, d displays the Fast Fourier transform (FFT) of the dHvA signal to extract the superimposed frequencies F. Many frequencies, and their harmonics, can be observed in the range 0–4 kT, which correspond to extremal cross-sectional areas of the different FS sheets, according to the Onsager relation, $F = \hbar/2\pi e \cdot A$, where A is the cross-sectional area, $\hbar$ is the reduced Planck constant and e the electron charge. The magnitude of selected frequencies as a function of the temperature are shown in Supplementary Fig. 3 in the SI file. The experimental data have been fitted using the temperature damping factor of the Lifshitz-

Kosevich formalism, i.e., $X/\sinh(X)$, where $X = 2\pi^2 k_B T m^\star/e\hbar\mu_0 H$, $m^\star$ is the carrier effective mass in units of the free electron mass m_e[51]. Supplementary Table 2 summarizes all the detected frequencies and their corresponding effective masses. As seen, all the experimentally obtained effective masses display values within the ~$0.08 - 0.24 m_e$, with those associated to the lower frequencies agreeing well with the theoretically predicted values. On the other hand, the theoretical band masses m_b associated with the higher frequencies are overestimated in comparison to the measured effective masses, indicating that the electronic bands yielding these FS sheets disperse more linearly than predicted by the calculations.

Interestingly, the amplitude of these dHvA frequencies is markedly angle dependent. For instance, the κ-branch reveals the existence of the so-called spin-zeros or angles where the magnitude of the oscillations vanishes due to the spin-dephasing factor in the Lifshitz-Kosevich formalism, i.e., $R_s = \cos(\pi g m^\star/2m_0)$, where g is the Landé g-factor[51]. This term reaches zero whenever $\pi g m^\star/2m_0 = (2n + 1)\pi/2$. Supplementary Fig. 7, displays the FFT magnitude of the κ-branch as a function of θ', revealing two spin-zeros from which one can estimate both the value and the anisotropy of the g-factor. To calculate the g-factor, we use two approaches, one based on DFT calculations and the other on experimental results. According to the theoretically calculated effective masses shown in Supplementary Fig. 8, at the first spin-zero occurring at $\theta' \sim 30°$, chosen by us to correspond to $n = 0$, one obtains $g \approx 1.96$. For the second at $\theta' \sim 80°$, or $n = 1$, one obtains $g \approx 5.26$. From Supplementary Fig. 8 it is evident that the
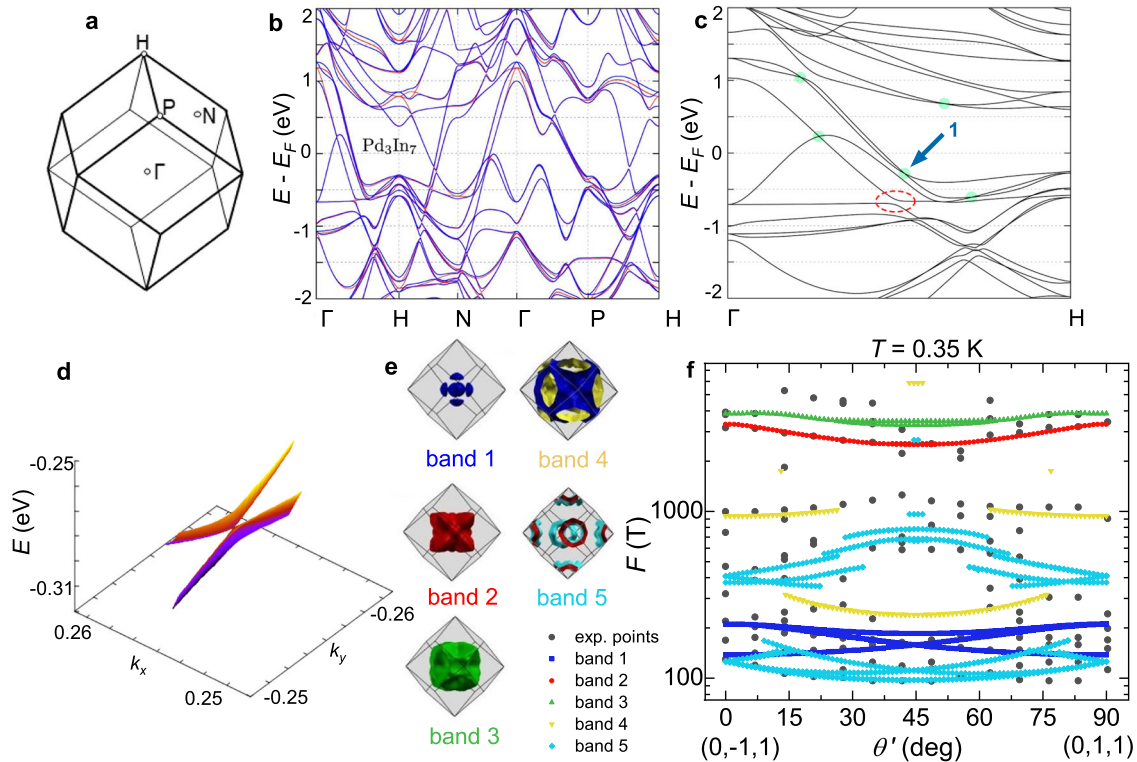
Fig. 5 Comparison between calculated and experimental Fermi surface cross-sectional areas. a First Brillouin zone (FBZ) of Pd_3In_7 indicating its high symmetry points and the high symmetry paths explored within its FBZ to evaluate its electronic band structure. **b** Theoretically calculated electronic band structure of Pd_3In_7 in the absence (orange lines) and presence (blue lines) of spin orbit coupling (SOC). **c** Electronic band structure of Pd_3In_7 along the Γ-H direction, revealing a number of degenerate crossings that lead to type-II Dirac nodes (indicated by green dots). Several crossings become gaped when the SOC is incorporated into the calculations (indicated by dashed red circle). **d** Three-dimensional plot of the band crossing labeled as 1 in panel c, revealing a type-II Dirac band touching. A few of these crossings were found to produce Dirac nodal lines. **e** Three-dimensional plots of the calculated Fermi surface sheets in the FBZ resulting from the distinct bands intersecting the Fermi level. **f** Comparison between the angular dependence of the experimental dHvA frequencies (gray dots) and the theoretically predicted (colored dots) Fermi surface cross-sectional areas of Pd_3In_7. Here, the colors of the markers were chosen to match those depicting each FS sheet. See, Supplementary Fig. 10 for a colored depiction of the individual bands leading to each of the plotted Fermi surfaces.

$m_\kappa^\star$ associated to the κ-branch does not change considerably as a function of θ'. In fact, even if we did not choose specific values for $m_\kappa^\star$, the values of g for the first spin-zero would fall within $1.64 \leq g \leq 2.04$, and $4.92 \leq g \leq 6.12$ for the second. The other approach is to use the experimentally obtained effective masses. In Supplementary Fig. 9 we provide values of $m_\kappa^\star$ for two angles, i.e., $\theta' = 0°$ and $40°$. The DFT calculations in Supplementary Fig. 8 imply that $m^\star$ does not change much within the range $\theta' = 30° - 60°$. Therefore, the experimental value of $m^\star$ at $\theta' = 40°$ can be safely used to estimate g at the first spin-zero, or $n = 0$, yielding $g = 9.1$. For the second spin-zero, or $n = 1$, the value of $m_\kappa^\star$ at $\theta' = 0°$ can be used, since our calculations indicate this value to be equal to the value of $m_\kappa^\star$ at $\theta' = 90°$. This effective mass value would yield $g = 17.64$. Regardless of the precise values used, one can safely conclude that the Landé g-factor in Pd_3In_7 is anisotropic and displays large values. Values that are considerably larger than the usual $g = 2$ value assumed for free electrons, pointing to a pronounced orbital contribution to g. The immediate consequence of a large and anisotropic g-factor, would be a very pronounced and anisotropic Zeeman-effect, capable of spin polarizing and therefore deforming the geometry of the smaller Fermi surfaces of Pd_3In_7. This, in turn, is likely to affect the scattering rates and hence carrier mobilities on the FS sheets.

Now we proceed to compare the geometry of the experimentally determined FS sheets with those resulting from our electronic band structure calculations. A good agreement between them would support the validity of the calculations, and hence the existence of Dirac nodes in Pd_3In_7. Figure 5a displays the first Brillouin zone of Pd_3In_7 along with its high symmetry points as well as high symmetry directions connecting them. The actual electronic band structure, along the main reciprocal lattice directions of Pd_3In_7, is shown in Fig. 5b and Supplementary Fig. 11. Blue lines depict calculations including spin-orbit coupling (SOC) while the orange ones exclude SOC. As seen in Fig. 5b, c, and Supplementary Fig. 11, one easily identify a total of five tilted Dirac type-II nodes along the $\Gamma - H$, $\Gamma - N$, and P-H directions that are within ± 250 meV from the Fermi level ε_F, with some of the associated bands dispersing linearly all the way up (or down) to ε_F. In Fig. 5c, the crossings leading to type-II Dirac nodes are indicated by green markers. Notice that several of the crossings observed in Fig. 5b become gaped by the SOC, as is illustrated in Fig. 5c by the red dashed line encircling two nearly touching bands. Other crossings lead to Dirac nodal lines (see, Supplementary Fig. 11). To illustrate the presence of multiple type-II Dirac nodes in this system, we show in Fig. 5d a three-dimensional plot of a specific crossing, or a type-II Dirac band touching, labeled as crossing 1 in Fig. 5c, which is relatively close to ε_F. See methods for calculation details.

Experimentally, the topography of the FS can be mapped out via the angular dependence of the dHvA frequencies. A good agreement between our observations and the theoretically predicted angle-dependent FS cross-sectional areas would support our calculations and therefore the existence of Dirac nodes close to ε_F in Pd_3In_7. Here, the fundamental question is if there is a

correlation between the type-II Dirac nodes and the anomalous magnetoresistivity displayed by Pd_3In_7. But first, we must confirm their presence by comparing calculated and experimentally determined FS geometries.

Colored panels, in Fig. 5e, display the FS sheets for the different bands intersecting ε_F. In Supplementary Fig. 10 the electronic band structure is displayed with the bands intersecting ε_F having different line colors to convey the respective bands that yield each of the FS sheets shown in Fig. 5e. While gray markers in Fig. 5f depict the angular dependence of the observed dHvA frequencies F, colored markers correspond to the theoretically calculated FS cross-sectional areas (in Fig. 5e). Bands 1 through 3 yield hole pockets, while bands 4 and 5 produce electron-like sheets. In Fig. 5f, there is a good agreement between the experimental and theoretical points for the high frequencies, or FS sheets, from bands 2 and 3. These hole pockets are the FSs with the largest volume relative to the volume of the Brillouin zone, and therefore they contribute the most to the density of carriers. For the smaller volume FS sheets (or lower frequencies), there are discrepancies between the theoretical and experimental points. In our experience, minor discrepancies between FSs determined through quantum oscillatory phenomena and those resulting from Density Functional Theory (DFT) calculations are rather common, see for example refs. [52,53]. One can understand this from the fact that different DFT implementations, for example using distinct electron-density functionals (GGA, PBE, HSE06, etc.), tend to yield slightly different positions for the electron and hole bands relative to ε_F. Therefore, we estimate the typical DFT error bar to be in the order of a few tens of meV, by comparing the distinct DFT implementations. However, such a small energy value, or small displacement relative to ε_F, can strongly impact the sizes of the smaller FS sheets.

In addition, multiple frequencies, harmonics and combinations of harmonics are observed due to the complexity of the calculated Fermi surface, and the high quality of the single crystals of Pd_3In_7 (Fig. 4c, d). This makes it challenging to distinguish fundamental frequencies from harmonics and their combinations. Therefore, we conclude that Fig. 5 points to a quite honest agreement between calculations and the experimental data, thus supporting the existence of Dirac type-II nodes in Pd_3In_7. This conclusion is further supported by the small effective masses tabulated in Supplementary Table 2, albeit they are not perfectly captured by the calculations that yield heavier masses for the larger Fermi surface sheets. This indicates that DFT overestimates the curvature of some of the bands in the vicinity ε_F. The small experimental quasiparticle effective masses, for all FS sheets, further support the notion of Pd_3In_7 being a Dirac like compound. Despite minor disagreements with the experiments, DFT reveals the presence of multiple type-II Dirac nodes in Pd_3In_7 near ε_F and this is crucial for interpreting our observations, as we outline below.

DISCUSSION

From the magnetoresistivity measurements we extracted four important observations: (i) it displays a linear in field behavior from $\mu_0H = 0$ T all the way up to the highest field value of $\mu_0H = 41$ T when $\theta = 0°$, (ii) for all other values of θ, the magnetoresistivity displays a superposition of linear plus quadratic in field terms that becomes sub-linear when μ_0H exceeds 4 T, with a power exponent as low as $n = 0.7$, (iii) for a metal characterized by large Fermi surface sheets (or, in contrast to nearly compensated semimetals), the magnetoresistivity is very large, reaching 10^4 % under $\mu_0H = 41$ T, and iv) its anisotropy leads to a butterfly like angular dependence that was previously reported for Dirac nodal line semimetals.

Linear CMR starting from very low magnetic fields was previously reported for the pnictide FeP[54], where a combination of topological band structure with helimagnetic order, led the

authors to propose intra-band scattering among topological bands for its origin. Linear CMR was also observed in high mobility semiconducting GaAs quantum wells[55] and ascribed to the so-called resistance rule, dictating that their magnetoresistivity should be proportional to the derivative of the Hall response with respect to the induction field B or $R_{xx} = dR_{xy}/dB \times B \times \alpha$, where α is a constant of proportionality. However, and as we show in Supplementary Fig. 12, $dR_{xy}/dB \times B$ is not at all linear for Pd_3In_7, indicating the irrelevance of this scenario for this compound. Linear CMR in the cuprates[56], and also in the Fe based superconductors[57], was attributed to the field-induced renormalization of the dynamics intrinsic to their quantum critical fluctuations (associated to suppression of their magnetic order) and hence of their concomitant quasiparticle lifetime. However, Pd_3In_7 is non-magnetic, does not exhibit long-range charge-order, and does not reveal evidence for pronounced electronic correlations due to a possible proximity to a quantum critical point. Therefore, these previously proposed mechanisms are unable to address its linear magnetoresistivity, which in contrast to these examples, is observed also for fields aligned along the electrical currents, or in a LMR configuration. Linear CMR was reported for Dirac and Weyl semimetals, like Cd_3As_2[9,58], NbP[32], TiBiSSe[59], graphene[60,61], topological insulators like YPdBi[62] or Bi_2Te_3 nanosheets[63], as well as charge/spin density-wave materials[64]. Given the observation of linear CMR in multiple Dirac/Weyl systems including Pd_3In_7, see Fig. 3c and d, one is led to conclude that linear in field magnetoresistivity is intrinsic to linearly dispersing electronic bands. Notice that linear LMR was previously reported for WTe_2[65], a compound also proposed to be a type-II Weyl semimetal[25]. Although, in contrast to Pd_3In_7, WTe_2 displays a quadratic in field CMR[31].

The theory of the quantum linear magnetoresistivity by Abrikosov[66], cannot be applied to Pd_3In_7. According to it, a very small Fermi surface pocket dominates the magnetoresistivity when it is driven to the quantum limit by an increasing field, or when all carriers fill the lowest Landau level. In our case, the observed as well as the calculated de Haas-van Alphen frequencies, exceed $\mu_0H = 100$ T, implying that during the measurements we remained far below the quantum limit for all Fermi surface sheets. In Cd_3As_2 the linear MR is attributed to the magnetic-field induced lifting of a proposed topological protection against backscattering[9,67] or to mobility fluctuations caused by disorder in this system[58]. We have no experimental evidence pointing to topological protection in Pd_3In_7. As for mobility fluctuations, it is very unlikely that such scenario would also explain its sublinear magnetoresistivity as the crystal is tilted, or the angular dependence of the power law exponent n. Instead, we discuss below the possible role of a large anisotropic Zeeman-effect on the geometry of the Fermi surface of Pd_3In_7 which we postulate to be a non-compensated metallic system. Notice that we cannot extract its carrier densities through fittings of our transport data to conventional transport models because these assume a quadratic in field behavior for the magnetoresistivity.

Pd_3In_7 has multiple type-II Dirac nodes (Fig. 5b, c, and Supplementary Fig. 11) dispersing along distinct directions within its Brillouin zone. Under a magnetic field, each type-II Dirac cone splits into type-II Weyl cones of opposite chirality due to the Zeeman effect. The vector connecting them is defined by both the Zeeman-effect and the spin-orbit coupling (SOC) acting on each band. Now, as the sample is rotated, the high Landé g-factor of the system can trigger a strong and anisotropic Zeeman response, modifying the geometry and hence the scattering rate on the FSs. As a result, the ratio between electron and hole mobilities (μ_e/μ_h) is likely to vary with the field. Now, as we show below, varying μ_e/μ_h for a system with uncompensated carrier density ($n_e/n_h \neq 1$) explains the linear as well as the sublinear dependence of the power-law exponent $n(\theta)$ of the CMR, even when these ratios are assumed to be field independent.
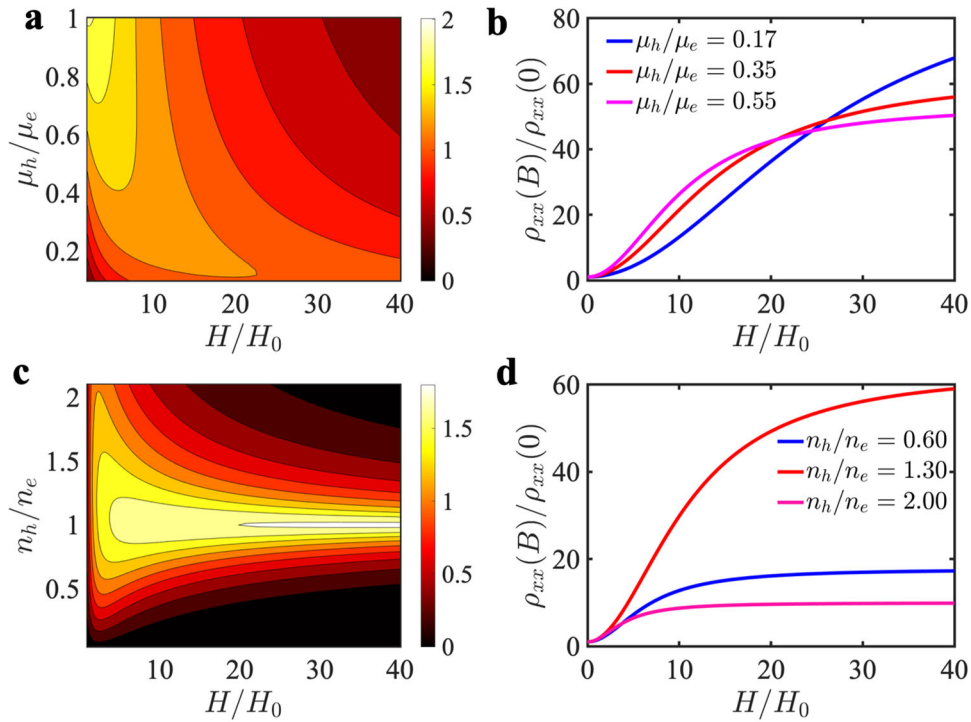
Fig. 6 Origin of the anomalous power law in the conventional magnetoresistivity. a Contour plot of the exponent n in the power-law dependence of the magnetoresistivity on the magnetic field ($\mu_0 H$), $\rho_{xx} \sim (\mu_0 H)^n$, evaluated after inverting Eq. (3) and for the ratio among carrier mobilities μ_h/μ_e ranging from ~0 to 1. μ_h and μ_e stand for hole and electron mobilities, respectively. Here, $\mu_0 H_0 \approx 1/\mu_e \approx 0.8$ T, which corresponds to magnetic fields ranging from 0 to 32 T. **b** Calculated resistivity ρ_{xx} as a function of the external magnetic field for different values of the ratio μ_h/μ_e. For panels (**a**) and (**b**), we chose $n_h/n_e = 0.75$. **c** Contour plot of n in the $\mu_0 H$ - n_h/n_e plane. It is clear that a marked difference in carrier mobilities, when coupled to even a small imbalance in carrier densities, can favor $n \leq 1$. **d** Calculated resistivity ρ_{xx} as a function of the magnetic field for different values of the ratio n_h/n_e. For panels (**c**) and (**d**), we choose $\mu_h/\mu_e = 0.50$.

To better emphasize our point, we consider a simple two-band model, for which the semiclassical conductivity is given by the following expression in complex representation[31]

$$\sigma = e \left[\frac{n_e \mu_e}{(1 + i\mu_e \mu_0 H)} + \frac{n_h \mu_h}{(1 - i\mu_h \mu_0 H)} \right], \tag{3}$$

where n_e and n_h are the carrier densities of electrons and holes, respectively, and μ_e and μ_h are their corresponding mobilities. Equation (3) can be inverted to find the resistivity ρ in complex representation. The real part of ρ provides ρ_{xx}.

In Fig. 6 the exponent n, corresponding to the power-law, $\rho_{xx} \sim (\mu_0 H)^n$ is plotted for the above two-band model. For illustrative purposes, in the color contour plot of n displayed in Fig. 6a, we assume that the electron and hole carriers are uncompensated by fixing $n_h/n_e = 0.75$, while allowing both the magnetic field and the mobility ratio μ_h/μ_e to vary. In Fig. 6b, we display a few traces leading to the color contour plot. The ratio $n_h/n_e = 0.75$ is not based on experimental values extracted from measurements on Pd$_3$In$_7$ since, as previously mentioned, one cannot satisfactorily fit its transport data to conventional transport models. In fact, when we attempted to fit the Hall conductivity to the two-band model, it tended to converge to very large, non-physical ratios for the electron and hole mobilities, and respective densities, suggesting that our interpretation is correct. It turns out that from Eq. (3) the behavior of the exponent n with respect to the magnetic field and the mobility ratio μ_h/μ_e is in general non-monotonic. The important observation is that the exponent n can fall below two and all the way to one (linear dependence) and even below one (sublinear dependence). In Fig. 6c and d, we maintained the mobility ratio fixed at $\mu_h/\mu_e = 0.5$ but varied the ratio n_h/n_e. As seen, the magnetoresistivity displays a sublinear dependence on the external field for all values of n_h/n_e. Experimentally, we

determine that $1/\mu_e \approx \mu_0 H_0 \approx 0.8$ T (Fig. 1d) corresponding to the magnetic field range from 0 to 32 T in Fig. 6.

Since varying the angle θ in Fig. 1b can change the mobility ratio μ_h/μ_e (k-dependent scattering rate on the Fermi surfaces), the angular behavior of the exponent $n(\theta)$ in Fig. 3c is explained. We do not have an explanation for the evolution of the power law prefactor α. We point out that sublinear magnetoresistivity was also detected in the type-II Dirac semimetal NiTe$_2$[36].

As seen through Fig. 5 and Supplementary Fig. 11, the spin orbit coupling gaps a series of linear band crossings, but it still leaves others ungapped. The DFT calculations indicate that there are two non-gapped type-II Dirac nodes along the $\Gamma - H$ direction, a third one along the $\Gamma - N$ direction, and a fourth one along the $P - H$ direction, all located within ~250 meV of ε_F. The calculations indicate that other bands, not associated to linear band crossings or Dirac like nodes, and therefore topologically trivial, also intersect ε_F. However, as previously discussed, there are no known mechanisms that would explain the linear LMR based on topologically trivial bands and associated Fermi surfaces. In contrast, and as we discuss below, there are published predictions correlating the linear LMR with the chiral anomaly among type-II Dirac nodes[28,30,68]. Given the absence of an alternative explanation, and the existence in a very clean system like Pd$_3$In$_7$ of several Dirac type-II like nodes near ε_F, the only possible conclusion is to attribute the linear LMR to the non-trivial topology of the associated bands, despite not being located exactly at ε_F.

In effect, when the magnetic field has a nonzero component in the direction of the electric field, as in Fig. 1a, the linear dependence on the magnetic field, as well as the sign of the positive and linear LMR can be understood purely due to chiral anomaly[28,30,68]. It was initially anticipated that the chiral anomaly contribution to the LMR is always negative and quadratic.

However, it was shown that the magnetoresistivity can be linear as well as positive for sufficient tilting of the Weyl cones in the direction of the magnetic field[28,30]. The change in the sign of the magnetoresistance, i.e., from negative to positive, results from a finite intervalley scattering. In the Supplementary Information, we explicitly show the emergence of positive linear magnetoresistance for a model of tilted Weyl fermions, see, Supplementary Discussion and Supplementary Fig. 13. Even though our calculation is restricted to Weyl cones with the tilting parameter less than unity, we expect the qualitative features to remain the same even for larger values of the tilt, as also shown in earlier works[26]. Here, we emphasize that for the LMR configuration, there is no Lorentz force acting on the charge carriers. Therefore, one cannot calculate the LMR using the semiclassical approach of Eq. 3 which yielded a power law inferior to 1 for the CMR. In the present case, the natural mechanism that would yield linear longitudinal magneto-resistivity, as observed by us, is the chiral anomaly among type-II tilted Weyl nodes in broad agreement with refs. [26,28,30]. However, a precise comparison with these models would require additional DFT calculations that consider the Zeeman-effect as well as the spin-orbit coupling. The goal would be to determine the precise k-space orientation of the vector(s) connecting the field-induced type-II Weyl nodes, and their relative orientation with respect to electric and magnetic fields.

It is frequently assumed that the Dirac/Weyl nodes should be located at, or in the vicinity of ε_F, for the axial anomaly to affect transport properties. However, this critical distance to ε_F is system specific, and hence band-structure dependent. This mechanism depends on the remnant texture of the Berry phase at ε_F, whose sources/sinks are the Dirac/Weyl nodes, and on the exact scattering mechanism(s) at ε_F within a given system. Without detailed calculations, that are beyond the scope of this manuscript, there is no reason to assume that a distance $\Delta E \simeq 250$ meV, with respect to ε_F, for the type-II Dirac nodes of Pd_3In_7, should preclude a role for the chiral anomaly. Furthermore, in lattice models for Weyl semimetallic systems with Weyl nodes located away from ε_F, several models predicted a pronounced role for the axial anomaly, see for example, ref. [69]. As for the linear magnetoresistivity observed in Fig. 3d, over the entire range of the angle ϕ, one must consider that the axial anomaly is predicted to play a predominant role even when a very small component of the electric field is aligned along the magnetic field[69,70]. These models consider not only the role of the inter-valley scattering and the tilting of the cones, but also the non-linearity of the electronic bands away from the Dirac/Weyl nodes[69,70]. The angular range in Fig. 3d encompasses two behavioral extremes ranging from linear CMR ($\phi = 0°$) to linear LMR ($\phi = 90°$). Therefore, it is not surprising that the superposition of both contributions still leads to linear magnetoresistivity at intermediary angles.

We conclude by stating that our observations indicate that two mechanisms affect the magneto-transport of Pd_3In_7, i.e., the i) axial anomaly among field-induced type-II Weyl nodes, and ii) a multi-band effect arising from an uncompensated metal subjected to a pronounced, and angle-dependent, scattering rate on its Fermi surface. The observation of linear LMR in two crystallographic distinct compounds, i.e., cubic Pd_3In_7 and orthorhombic WTe_2[65], indicates that it is intrinsically associated to the type-II Dirac nodes in their electronic dispersion. Anisotropy in the scattering rate might result from a large and anisotropic Zeeman effect or, the large and anisotropic Landé g-factor of Pd_3In_7. Or, it might be intrinsic to systems lacking Lorentz invariance, as is the case for type-II Weyl/Dirac systems, implying that our observations might be generic and extendable to other systems. Even though linear LMR and sublinear CMR, have been previously and independently observed in Weyl semimetals, their simultaneous observation in a single system is the distinct hallmark of this work.

METHODS

Sample synthesis

High quality single crystals of Pd_3In_7 were synthesized via an In-flux method, where elemental Pd and In, with an atomic ratio 14:86, were loaded in a Al_2O_3 crucible and sealed in an evacuated fused silica ampule. The tube was heated to 750 °C and held there for 48 h. Then, it was cooled to 600 °C at a rate of 4 °C/h and afterwards slowly cooled to 400 °C at a rate of 0.5 °C/h. At this point, the tube was centrifuged and the as-harvested single crystals were etched in diluted HCl to remove residual metal from their surface. The result was the synthesis of shiny crystals with dimensions up to 2 mm.

Sample characterization

The chemical composition of the crystals was determined using single-crystal x-ray diffraction (SCXRD) spectroscopy. Face indexing of the single crystal was performed at room-temperature using a Rigaku-Oxford Diffraction Synergy-S single-crystal diffractometer equipped with a HyPix detector and a monochromated Mo-Kα radiation source ($\lambda = 0.71073$ Å). The data set was recorded as a series of ω-scans at 0.5° step width. The unit cell determination and face indexing were performed with the CrysAlis software package[71].

Magnetotransport measurements

For the magnetotransport measurements a Physical Property Measurement System (PPMS) in combination with a rotating probe was used under magnetic fields up to $\mu_0 H = 9$ T and temperatures as low as $T = 1.8$ K to perform a four-terminal resistivity measurements. Additional magnetotransport measurements, as well as the angular dependence of the dHvA effect using a piezoresitive microcantilever, were performed under continuous magnetic fields up to $\mu_0 H = 41.5$ T in a resistive Bitter magnet at the National High Magnetic Field Laboratory. The magnet was coupled to a ^{3}He cryostat allowing us to perform measurements at temperatures as low as $T = 0.35$ K.

Electronic band structure calculations

The first-principles (DFT) calculations were preformed using the projector augmented-wave (PAW) potentials[72] implemented in the Vienna Ab initio Simulation Package (VASP) code[73–75]. The calculations were performed in the absence and presence of the spin-orbit coupling (SOC) within the generalized gradient approximation (GGA) developed by Perdew, Burke, and Enzerhof (PBE)[76]. The energy cutoff for the plane-wave expansion is set to 350 eV. The electronic DOS was calculated using $15 \times 15 \times 15$ **k**–point grids in the Monkhorst–Pack scheme[77]. The Fermi surface was rendered using XCRYSDEN[78]. The frequencies of the Fermi surface were calculated using the Skeaf platform[79].

DATA AVAILABILITY

Relevant data supporting the key findings of this study are available within the article and the Supplementary Information file. All raw data generated during the current study are available from the corresponding authors upon request.

CODE AVAILABILITY

Relevant code for data analysis, data plotting, and band structure calculations are commercially sourced, e.g., the VASP code. Code used to calculated the magnetoresistivity as a function carrier densities and/or mobilities, or to calculate the magnetoresistivity as a function of magnetic field for a Weyl system characterized by tilted Dirac/Weyl cones, and inter-valley scattering, is available from the authors upon request.

REFERENCES

1. Qi, X.-L. & Zhang, S.-C. Topological insulators and superconductors. *Rev. Mod. Phys.* **83**, 1057–1110 (2011).
2. Wang, Z. et al. Dirac semimetal and topological phase transitions in A_3Bi ($A = Na$, K, Rb). *Phys. Rev. B* **85**, 195320 (2012).
3. Liu, Z. K. et al. Discovery of a three-dimensional topological Dirac semimetal, Na_3Bi. *Science* **343**, 864–867 (2014).
4. Lv, B. Q. et al. Experimental discovery of Weyl semimetal TaAs. *Phys. Rev. X* **5**, 031013 (2015).
5. Xu, S.-Y. et al. Discovery of a Weyl fermion semimetal and topological Fermi arcs. *Science* **349**, 613–617 (2015).
6. Schindler, F. et al. Higher-order topological insulators. *Sci. Adv.* **4**, eaat0346 (2018).
7. Balatsky, A. V., Vekhter, I. & Zhu, J.-X. Impurity-induced states in conventional and unconventional superconductors. *Rev. Mod. Phys.* **78**, 373–433 (2006).
8. Castro Neto, A. H., Guinea, F., Peres, N. M. R., Novoselov, K. S. & Geim, A. K. The electronic properties of graphene. *Rev. Mod. Phys.* **81**, 109–162 (2009).
9. Liang, T. et al. Ultrahigh mobility and giant magnetoresistance in the Dirac semimetal Cd_3As_2. *Nat. Mater.* **14**, 280–284 (2015).
10. Huang, H., Zhou, S. & Duan, W. Type-II Dirac fermions in the $PtSe_2$ class of transition metal dichalcogenides. *Phys. Rev. B* **94**, 121117(R) (2016).
11. Noh, H.-J. et al. Experimental realization of type-II Dirac fermions in a $PdTe_2$ superconductor. *Phys. Rev. Lett.* **119**, 016401 (2017).
12. Yan, M. et al. Lorentz-violating type-II Dirac fermions in transition metal dichalcogenide $PtTe_2$. *Nat. Commun.* **8**, 257 (2017).
13. Ma, Q. et al. Direct optical detection of Weyl fermion chirality in a topological semimetal. *Nat. Phys.* **13**, 842–847 (2017).
14. Wu, L. et al. Giant anisotropic nonlinear optical response in transition metal monopnictide Weyl semimetals. *Nat. Phys.* **13**, 350–355 (2017).
15. Rees, D. et al. Helicity-dependent photocurrents in the chiral Weyl semimetal RhSi. *Sci. Adv.* **6**, eaba0509 (2020).
16. Xu, S.-Y. et al. Electrically switchable Berry curvature dipole in the monolayer topological insulator WTe_2. *Nat. Phys.* **14**, 900–906 (2018).
17. Ma, Q. et al. Observation of the nonlinear Hall effect under time-reversal symmetric conditions. *Nature* **565**, 337–342 (2019).
18. Adler, S. L. Axial-vector vertex in spinor electrodynamics. *Phys. Rev.* **177**, 2426–2438 (1969).
19. Bell, J. & Jackiw, R. A PCAC Puzzle - $\pi^0 \to \gamma\gamma$ in σ-Model. *Il Nuovo Cim. A* **60**, 47–61 (1969).
20. Goswami, P., Pixley, J. H. & Das Sarma, S. Axial anomaly and longitudinal magnetoresistance of a generic three-dimensional metal. *Phys. Rev. B* **92**, 075205 (2015).
21. Huang, X. et al. Observation of the chiral-anomaly-induced negative magnetoresistance in 3D Weyl semimetal TaAs. *Phys. Rev. X* **5**, 031023 (2015).
22. Zhang, C.-L. et al. Signatures of the Adler-Bell-Jackiw chiral anomaly in a Weyl fermion semimetal. *Nat. Commun.* **7**, 10735 (2016).
23. Liang, S. et al. Experimental tests of the chiral anomaly magnetoresistance in the Dirac-Weyl semimetals Na_3Bi and GdPtBi. *Phys. Rev. X* **8**, 031002 (2018).
24. Burkov, A. A. & Kim, Y. B. Z_2 and chiral anomalies in topological Dirac semimetals. *Phys. Rev. Lett.* **117**, 136602 (2016).
25. Soluyanov, A. A. et al. Type-II Weyl semimetals. *Nature* **527**, 495–498 (2015).
26. Sharma, G., Goswami, P. & Tewari, S. Chiral anomaly and longitudinal magnetotransport in type-II Weyl semimetals. *Phys. Rev. B* **96**, 045112 (2017).
27. Zyuzin, V. A. Magnetotransport of Weyl semimetals due to the chiral anomaly. *Phys. Rev. B* **95**, 245128 (2017).
28. Morishima, K. & Kondo, K. General formula of chiral anomaly for type-I and type-II Weyl semimetals. *Appl. Phys. Lett.* **119**, 131907 (2021).
29. Zhang, K., Zhang, E., Xia, M., Gao, P. & Zhang, S. The axial anomaly in chiral tilted Weyl semimetals. *Ann. Phys.* **394**, 1–16 (2018).
30. Ahmad, A. & Sharma, G. Longitudinal magnetoconductance and the planar Hall effect in a lattice model of tilted Weyl fermions. *Phys. Rev. B* **103**, 115146 (2021).
31. Ali, M. N. et al. Large, non-saturating magnetoresistance in WTe_2. *Nature* **514**, 205–208 (2014).
32. Shekhar, C. et al. Extremely large magnetoresistance and ultrahigh mobility in the topological Weyl semimetal candidate NbP. *Nat. Phys.* **11**, 645–649 (2015).
33. Zhang, S. et al. Scaling of Berry-curvature monopole dominated large linear positive magnetoresistance. *Proc. Natl Acad. Sci. USA* **119**, e2208505119 (2022).
34. Xu, C. et al. Topological type-II Dirac fermions approaching the Fermi level in a transition metal dichalcogenide $NiTe_2$. *Chem. Mater.* **30**, 4823–4830 (2018).
35. Hu, Z. et al. Robust three-dimensional type-II Dirac semimetal state in SrAgBi. *npj Quant. Mater.* **8**, 20 (2023).
36. Zheng, W. et al. Bulk fermi surfaces of the Dirac type-II semimetallic candidate $NiTe_2$. *Phys. Rev. B* **102**, 125103 (2020).
37. Malavi, P., Kumar, P., Jakhar, N., Singh, S. & Karmakar, S. Signature of superconducting onset in presence of large magnetoresistance in type-II Dirac semimetal candidate Ir_2In_8S. *N. J. Phys.* **24**, 102002 (2022).
38. Zhang, H. et al. Thermoelectric properties of $Mo_3Sb_{5.4}Te_{1.6}$ and $Ni_{0.06}Mo_3Sb_{5.4}Te_{1.6}$. *J. Electron. Mater.* **36**, 727–731 (2007).
39. Bukowski, Z., Badurski, D., Stepien-Damm, J. & Troc, R. Single crystal growth and superconductivity of Mo_3Sb_7. *Solid State Commun.* **123**, 283–286 (2002).
40. Vergniory, M. G. et al. A complete catalogue of high-quality topological materials. *Nature* **566**, 480–485 (2019).
41. Flessa Savvidou, A. et al. Complex Dirac-like electronic structure in atomic site-ordered $Rh_3In_{3.4}Ge_{3.6}$. *Chem. Mater.* **33**, 1218–1227 (2021).
42. Pippard, A. *Magnetoresistance in Metals* (Cambridge University Press., 1989).
43. Pippard, A. Longitudinal magnetoresistance. *Proc. R. Soc. A: Math. Phys. Eng. Sci.* **282**, 464–484 (1964).
44. Zhou, Q. et al. Hall effect within the colossal magnetoresistive semimetallic state of $MoTe_2$. *Phys. Rev. B* **94**, 121101(R) (2016).
45. Schönemann, R. et al. Fermi surface of the Weyl type-II metallic candidate WP_2. *Phys. Rev. B* **96**, 121108(R) (2017).
46. Chiu, Y.-C. et al. Origin of the butterfly magnetoresistance in a Dirac nodal-line system. *Phys. Rev. B* **100**, 125112 (2019).
47. Husmann, A. et al. Megagauss sensors. *Nature* **417**, 421–424 (2002).
48. Kohler, M. Zur magnetischen widerstandsänderung reiner metalle. *Ann. Phys.* **424**, 211–218 (1938).
49. Leahy, I. A. et al. Nonsaturating large magnetoresistance in semimetals. *Proc. Natl Acad. Sci. USA* **115**, 10570–10575 (2018).
50. Ali, M. N. et al. Butterfly magnetoresistance, quasi-2D Dirac Fermi surface and topological phase transition in ZrSiS. *Sci. Adv.* **2**, e1601742 (2016).
51. Shoenberg, D. *Magnetic Oscillations in Metals*, Cambridge Monographs on Physics (Cambridge University Press, 1984).
52. Klotz, J. et al. Electronic band structure and proximity to magnetic ordering in the chiral cubic compound CrGe. *Phys. Rev. B* **99**, 085130 (2019).
53. Mozaffari, S. et al. Multiple Dirac nodes and symmetry protected Dirac nodal line in orthorhombic α-RhSi. *Phys. Rev. B* **102**, 115131 (2020).
54. Campbell, D. J. et al. Topologically driven linear magnetoresistance in helimagnetic FeP. *npj Quantum Mater.* **6**, 38 (2021).
55. Khouri, T. et al. Linear magnetoresistance in a quasifree two-dimensional electron gas in an ultrahigh mobility gaas quantum well. *Phys. Rev. Lett.* **117**, 256601 (2016).
56. Giraldo-Gallo, P. et al. Scale-invariant magnetoresistance in a cuprate superconductor. *Science* **361**, 479–481 (2018).
57. Hayes, I. M. et al. Scaling between magnetic field and temperature in the high-temperature superconductor $BaFe_2(As_{1-x}P_x)_2$. *Nat. Phys.* **12**, 916–919 (2016).
58. Narayanan, A. et al. Linear magnetoresistance caused by mobility fluctuations in n-doped Cd_3As_2. *Phys. Rev. Lett.* **114**, 117201 (2015).
59. Novak, M., Sasaki, S., Segawa, K. & Ando, Y. Large linear magnetoresistance in the Dirac semimetal TlBiSSe. *Phys. Rev. B* **91**, 041203 (2015).
60. Friedman, A. L. et al. Quantum linear magnetoresistance in multi layer epitaxial graphene. *Nano Lett.* **10**, 3962–3965 (2010).
61. Kisslinger, F. et al. Linear magnetoresistance in mosaic-like bilayer graphene. *Nat. Phys.* **11**, 650–653 (2015).
62. Wang, W. et al. Large linear magnetoresistance and Shubnikov-de Hass oscillations in single crystals of YPdBi heusler topological insulators. *Sci. Rep.* **3**, 2181 (2013).
63. Wang, X., Du, Y., Dou, S. & Zhang, C. Room temperature giant and linear magnetoresistance in topological insulator Bi_2Te_3 nanosheets. *Phys. Rev. Lett.* **108**, 266806 (2012).
64. Feng, Y. et al. Linear magnetoresistance in the low-field limit in density wave materials. *Proc. Natl Acad. Sci. USA* **116**, 11201–11206 (2019).
65. Zhao, Y. et al. Anisotropic magnetotransport and exotic longitudinal linear magnetoresistance in WTe_2 crystals. *Phys. Rev. B* **92**, 041104 (2015).
66. Abrikosov, A. A. Quantum magnetoresistance. *Phys. Rev. B* **58**, 2788–2794 (1998).
67. Feng, J. et al. Large linear magnetoresistance in Dirac semimetal Cd_3As_2 with fermi surfaces close to the Dirac points. *Phys. Rev. B* **92**, 081306 (2015).
68. Knoll, A., Timm, C. & Meng, T. Negative longitudinal magnetoconductance at weak fields in Weyl semimetals. *Phys. Rev. B* **101**, 201402 (2020).
69. Sharma, G., Goswami, P. & Tewari, S. Nernst and magnetothermal conductivity in a lattice model of Weyl fermions. *Phys. Rev. B* **93**, 035116 (2016).
70. Sharma, G., Nandy, S. & Tewari, S. Sign of longitudinal magnetoconductivity and the planar hall effect in Weyl semimetals. *Phys. Rev. B* **102**, 205107 (2020).
71. CrysAlis. Oxford diffraction limited. *Abingdon, England* (2006).
72. Blöchl, P. E. Projector augmented-wave method. *Phys. Rev. B* **50**, 17953 (1994).
73. Kresse, G. & Hafner, J. Ab initio molecular-dynamics simulation of the liquid-metal-amorphous-semiconductor transition in germanium. *Phys. Rev. B* **49**, 14251 (1994).

74. Kresse, G. & Furthmüller, J. Efficient iterative schemes for ab initio total-energy calculations using a plane-wave basis set. *Phys. Rev. B* **54**, 11169 (1996).

75. Kresse, G. & Joubert, D. From ultrasoft pseudopotentials to the projector augmented-wave method. *Phys. Rev. B* **59**, 1758 (1999).

76. Perdew, J. P., Burke, K. & Ernzerhof, M. Generalized gradient approximation made simple. *Phys. Rev. Lett.* **77**, 3865–3868 (1996).

77. Monkhorst, H. J. & Pack, J. D. Special points for brillouin-zone integrations. *Phys. Rev. B* **13**, 5188–5192 (1976).

78. Kokalj, A. XCrySDen-a new program for displaying crystalline structures and electron densities. *J. Mol. Grap. Model.* **17**, 176–179 (1999).

79. Rourke, P. & Julian, S. Numerical extraction of de Haas-van Alphen frequencies from calculated band energies. *Comput. Phys. Commun.* **183**, 324–332 (2012).

ACKNOWLEDGEMENTS

AUTHOR CONTRIBUTIONS

A.F.S. and L.B. conceived and led the project. A.F.S. synthesized the samples and performed the transport measurements. A.F.S., B.C., and L.B. performed the high field measurements. A.F.S. analyzed all the experimental data. A.P. performed the theoretical calculations for the electronic structure and the Fermi surface. A.F.S. performed the calculations for the different frequencies of the Fermi surface. J.C., V.L., and M.S. performed the single crystal XRD analysis. G.S. and S.T. proposed the model explaining the linear and sublinear (in magnetic field) conventional magnetoresistivity, as well as the linear longitudinal magnetoresistivity. A.F.S. and L.B. prepared the manuscript with input from all co-authors.

COMPETING INTERESTS

The authors declare no competing interests.

ADDITIONAL INFORMATION

Supplementary information The online version contains supplementary material available at https://doi.org/10.1038/s41535-023-00601-7.

Correspondence and requests for materials should be addressed to Luis Balicas.

Reprints and permission information is available at http://www.nature.com/reprints

Publisher's note Springer Nature remains neutral with regard to jurisdictional claims in published maps and institutional affiliations.